Fault Rupture Propagation in Alluvium and Its Interaction with Foundation: New Insights from 1g Modelling via High Resolution Optical Image Processing Techniques

Meysam Fadaee[1]*, Mohammad Kazem Jafari[2], Mohsen Kamalian[3], and Seyed Alireza Mustafa[4]

1. PhD Candidate, International Institute of Earthquake Engineering and Seismology (IIEES), Iran, * Corresponding Author; email: m.fadaie@iiees.ac.ir
2. Professor, Geothecnic Research Center, International Institute of Earthquake Engineering and Seismology (IIEES), Iran
3. Associate Professor, Geothecnic Research Center, International Institute of Earthquake Engineering and Seismology (IIEES), Iran
4. Basir Pardazan Sanat Ltd. and Research Assistant of International Institute of Earthquake Engineering and Seismology (IIEES), Iran

ABSTRACT

Earthquake fault ruptures may emerge at the ground surface causing large differential movements. Fault ruptures can cause significant damage when they emerge at or adjacent to the position of existing foundation. However, the study of recent faulting events revealed that, in some circumstances, the fault-rupture emergence is affected by the presence of buildings. A 1g modelling study, as well as validated numerical modelling was conducted to investigate how reverse faults interact with strip foundations which run parallel to the fault strike. To better understand this process, we monitor displacement field in scaled model experiments using high-resolution optical image correlation techniques. High-resolution optical strain monitoring quantifies the spatial pattern of strain accumulation in our model experiments. In this paper, following the explanation of 1g model test apparatus, the steps leading to development of an image processing program are described. Afterwards, by using this tool, we investigate the interaction between fault rupture and foundation. This study confirms that fault rupture may be deviated by the foundation so that the foundation is protected from serious rotations and detachment.

1. Introduction

During earthquakes, both transient ground shaking and permanent ground deformation are produced. Up to now, most researches have concentrated on the performance of structures during transient ground shaking. However, in large-magnitude earthquakes, the fault rupture may spread to the surface, imposing considerable deformation to overlaying structures. Recent Earthquakes have shown that faulting can cause extensive damage to different structures [1-2].

One of the most important examples of the fault rupture hazard was occurred by the 1999 Chi-Chi earthquake in Taiwan. The total length of rupture was almost 90 km caused by Mw 7.6 earthquake. Vertical fault scarps reached up to 10 m at some points. Many case histories of fault rupture interaction with engineering structures can be found in the related literature. In Wenchuan earthquake (2008) with Mw 7.8 in China, three major seismic faults ruptured simultaneously, and propagated to the ground surface,

leading to a surface fault outcrop of 285 km in length - the longest ever recorded [3-4]. The earthquake is a very important seismic event, full of case histories related to fault rupture and its interaction with structures.

The research in the field of fault rupture foundation interaction was carried out in three fields: a) Investigating the case histories in past earthquakes [1, 5, 6], b) physical modelling including 1 g tests [6-7] and centrifuge model tests [8-9], and finally c) numerical analyses [5, 10, 11, 12]. All these works lead to reliable numerical tools as well as physical models which capture important aspect of this problem. All these researches have proven that foundation system and its bearing pressure are two important aspects of fault rupture foundation interaction.

This paper reports a study using 1g modelling to investigate the performance of shallow foundations resting on shallow soil layers subject to reverse faulting. To this end, the emphasis is placed on the measurement of soil displacement fields and foundation movements, which are achieved by use of digital image analysis. Even measuring gross or ultimate deformations through comparative pre- and post-test observations provides insight into the ultimate failure mechanism of fault rupture and ground surface profile as well as the shear strain in soil media [13]. The image processing technique employed in this paper can measure incremental deformation and progression of the fault rupture and ground surface profile. Digital images of the soil sample were captured through the Plexiglas front face using a professional digital camera facing the apparatus. As the faulting tests proceeded, a series of up to 80 digital images were collected, each corresponding to a different fault displacement. By evaluating the sequences of the digital images captured in time, displacement and strain fields of soil can be computed with digital image processing. Comparing the experimental results from image processing by numerical analysis, the importance of foundation bearing pressure in fault rupture deviation was investigated. It was observed that the rupture can be diverted using heavy-bearing pressure foundation.

2. Problem Definition and Methodology

The aim of the work presented herein is to study the influence of foundation surcharge on fault

rupture. The investigated problem is schematically illustrated in Figure (1). We consider a uniform sand deposit of depth $H = 20$ m, at the base of which a thrust fault with a dip angle $\alpha = 45°$ produces upward displacement of vertical amplitude h. A stiff raft foundation of width $B = 15$ m carrying a surcharge load q, is positioned at distance $s/B = 0.3$ from the point of rupture outcropping in the free field. To assess the influence of the load, two foundations are tested and compared. The increasing of the load will lead to fault rupture diversion, and substantial reduction of foundation rotation.

A combination of experimental and numerical work is used to strengthen the validity of the inferred conclusions. Reduced-scale physical model testing is conducted for validation of numerical models.

2. Physical Modelling (1g Tests)

1g tests were conducted at the Geotechnical Engineering Research Centre of the International Institute of Earthquake Engineering and Seismology (IIEES) in Iran, using a custom built split-box capable of simulating dip slip (i.e. normal and reverse)
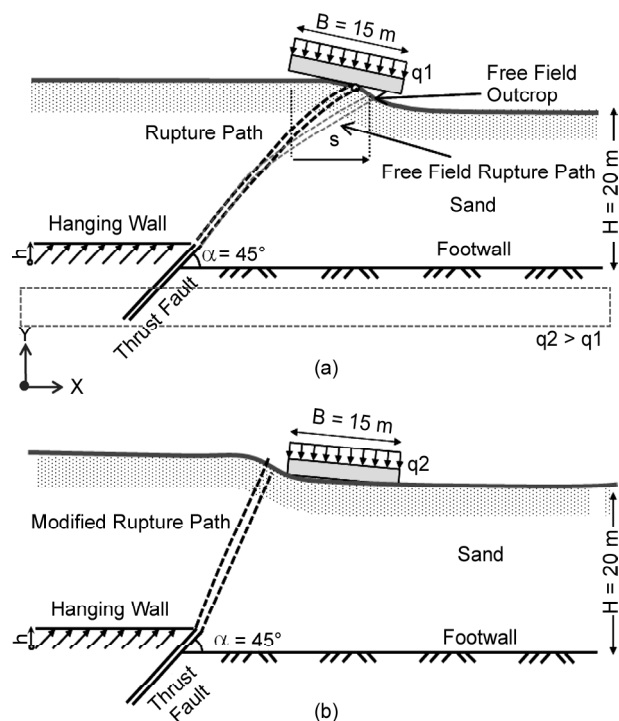

Figure 1. Sketch of the problem and its geometry: (a) interaction of a thrust fault rupture, propagating through an H = 20 m soil deposit, with a slab foundation of width B, carrying a surcharge load q, positioned at distance s from the theoretical point of rupture outcropping in the free field; and (b) placement of heavier bearing pressure foundation leads to fault rupture diversion.

faulting and its interaction with strip foundations [6]. The split-box is 180 cm in length and 50 cm in width, allowing a maximum soil depth of 50 cm. An electric actuator was used to push the movable part (0.4 m in length) of the apparatus (representing the hanging wall) up or down, simulating reverse and normal faulting, respectively. The dip angle α of the fault is adjustable, and a value of 45°, which is considered a representative for thrust faults, was used for the experiments reported herein. To allow direct observation of the deformed soil specimen, two Plexiglas windows were installed at the two faces of the split-box. Taking account of minimum depth required for reasonable results [7], a scale of $N = 100$ was selected for the experiments (i.e. the $H = 20$ m prototype soil was modelled as a 20 cm soil layer in the experiment). Since the main scope of the experiments in this paper is to investigate the influence of foundation surcharge on fault rupture, the $B = 15$ cm foundation (corresponding to the 15 m prototype), made of Perspex, is selected. In Figure (2) the faulting apparatus (split-box) and camera are shown. The tests were conducted under quasi-static conditions (i.e. at a slow velocity). Digital images of the deformed soil specimen were captured after every 2 mm of imposed bedrock offset using a high-resolution (8 mega pixel) digital camera.

The 20 cm deep soil layer was prepared by dry air pluviation of No. 161 Firoozkooh sand: a (relatively) uniform fine sand with a mean grain size $d_{50} = 0.25$ mm, specific weight $G_s = 2.61$, and minimum and maximum dry density 1.71 g/cm³, and 1.42 g/cm³, respectively. The grain size distribution

Figure 2. photo of the faulting apparatus (split-box), camera and DC.

is shown in Figure (3). The sand was pluviated from a specific height with a fixed sieve aperture to control the mass flow rate, giving a uniform density $Dr \approx 80\%$.
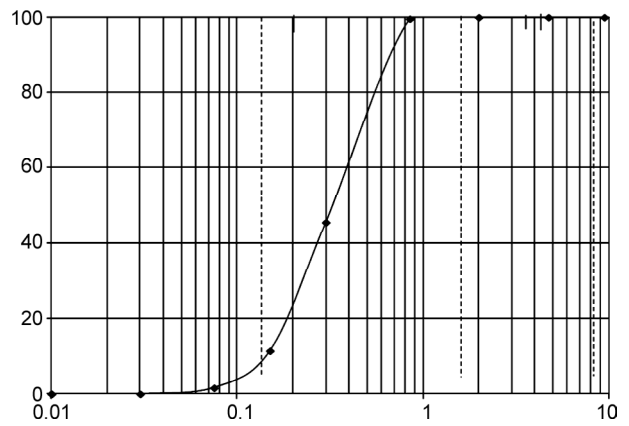

Figure 3. Grain size distribution of tested sand.

The same sand, dyed blue, was used as a marker at the two side walls of the split-box. Direct shear tests were conducted to measure the peak and residual strength of the sand. For $\sigma_v \geq 100$ kPa (representative for the prototype), the peak and residual friction angles were $\varphi_{peak} = 42°$ and $\varphi_{res} = 31°$, while the dilation angle Ψ, which depends significantly on the effective stress, was approximately 10° for the same normal stress. For low normal stress, $\sigma_v < 10$ kPa, which is more representative of the stress level existing in the reduced-scale tests, the peak friction angle increases considerably, reaching $\varphi_{peak} \approx 49°$, see also [14].

3. Image Processing Techniques

The sequence of images is obtained using a high-resolution camera under controlled lighting condition. Assuming a pinhole camera model and division model for lens/glass distortion, the camera is first calibrated and the image sequence is rectified using the derived optical parameters of the whole system. By computing the optical flow between each pair of consecutive rectified images of the sequence, the relative motion of sand particles is tracked in time and space. By tracing the relative motion back to the initial image, we can compute the absolute position of sand particles.

Using a Lagrangian description for modelling particulate motion path, absolute positions of sand particles are used to obtain the strain field across the

image domain. With constant-strain triangular (CST) elements, the absolute displacement field is automatically converted to strain field. Both formulae of small deformation and infinitesimal strain theories in Lagrangian description are given for the CST element. A commercial software package (VSG for vision strain gauge) is developed to ease the process from calibration to strain/displacement field computations and export of the numerical results to Excel.

The sequence of described image processing techniques is as follows: Section 3.1 describes the basic camera calibration procedure. Section 3.2 gives an outline of optical flow method and its application to motion estimation. In section 3.3, we show how the estimated motion may be used to derive the strain field.

3.1. Camera calibration

Camera calibration is the first step toward recovering metric information from 2D images. In computer vision, the standard method for camera calibration is to observe a calibration object with known geometry in 3D space from multiple views. In our problem, the calibration object is a plate with points of known metric position.

Having determined the local position of all points on the calibration plate, we can form a set of equations that map the image points to world coordinates. Therefore, the image is said to be calibrated.

The camera calibration process yields two sets of parameters known as intrinsic and extrinsic parameters of the camera. Intrinsic or interior parameters refer to camera configuration that includes focal length, optical centre of lens, lens distortion, and size of its imaging sensor. The extrinsic or external parameters define the spatial position and orientation of the camera with respect to the world coordinate system. World coordinate system is typically placed on the calibration object. To better understand the calibration procedure, the transformation of a single object point with respect to world coordinate system to image plane must be studied.

Any point in 3D world coordinate system goes through the following four steps to form an image point, see Figure (4): first, transformation from world coordinate system (WCS) to camera coordinate system (CCS); second, projection from CCS to
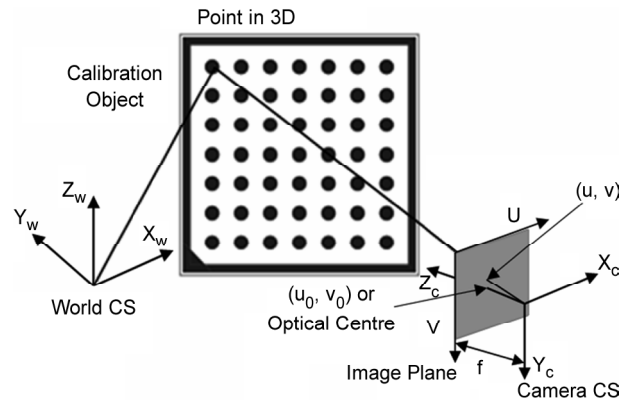

Figure 4. Photo of the faulting apparatus (split-box), camera and DC.

image coordinate system (ICS); third, lens distortion modifying image points in radial/tangential directions; fourth, transformation of image point into discrete image pixels. These steps are described below, as graphically depicted in Figure (4):

i) Rigid transformation from world CS to camera CS:

$$\bar{p}^c = R^c \bar{p}^w + \bar{t}^c \tag{1}$$

where $\bar{p}^c = [x^c, y^c, Z^c]^T$ is the point location in CCS, $\bar{p}^w = [x^w, y^w, z^w]^T$ is the point location in WCS, and $R^c, \bar{t}^c$ are the rotation matrix and translation vector between the two coordinate frames, respectively. This transformation has six degrees of freedom (DOF) and defines the exterior camera calibration parameters.

ii) Perspective projection of $\bar{p}^c = [x^c, y^c, x^c]^T$ onto $\bar{p}_i = [u, v]^T$ in the imaging sensor plane, assuming an ideal pinhole model for the camera where (f is the camera focal length):

$$\begin{pmatrix} u \\ v \end{pmatrix} = \frac{f}{z^c} \begin{pmatrix} x^c \\ y^c \end{pmatrix} \tag{2}$$

iii) Lens distortion: the points mapped into the image plane deviate from their ideal projections due to lens imperfections and aberrations. These effects lead to tangential (u_t, v_t) and radial distortions (u_r, v_r):

$$u_d = u + u_r + u_t$$

$$v_d = v + v_r + v_t \tag{3}$$

Note that the division model used for our purpose is a one-parameter (κ) equation for modelling the radial distortion:

$$u_d = \frac{2u}{1 + \sqrt{1 - 4\kappa(u^2 + v^2)}}$$

$$v_d = \frac{2v}{1 + \sqrt{1 + 4\kappa(u^2 + v^2)}} \qquad (4)$$

The Figure (5) shows the effect of parameter κ on the image of a calibration object.

iv) Transformation of image points from metric unit to pixel unit:

$$\begin{pmatrix} r \\ c \end{pmatrix} = \begin{pmatrix} \frac{v_d}{S_y} + C_y \\ \frac{u_d}{S_x} + C_x \end{pmatrix} \qquad (5)$$

where S_x, S_y represent the horizontal and vertical spacing of the sensor elements and C_x, C_y is the location of the optical centre of the lens projected onto the camera sensor or equivalently the centre of radial distortions.

The overall point transformations may be written in the following compact form:

$$\begin{pmatrix} r \\ c \end{pmatrix} = H \begin{pmatrix} x \\ y \\ z \end{pmatrix} \qquad (6)$$

where H represents the overall transformations

function. There are six unknown intrinsic parameters and six unknown extrinsic parameters in H. Having at least 12 equations is sufficient to find these parameters. However, to obtain a more accurate result, we augment the number of equations by including more pictures taken at different views from the calibration plate. This leads to an over determined system of nonlinear equations. To solve the equation for unknown calibration parameters, a nonlinear optimization process is required. The problem is formulated as minimization of the total least square errors of the transformed points on the calibration plate and the corresponding image points. At this point, we minimize the computational error between the observed image positions and the predicted positions based on the estimated calibration parameters H_p [15].

$$e^2 = \sum \left((r - r_p)^2 + (c - c_p)^2 \right) \qquad (7)$$

where $\begin{pmatrix} r_p \\ c_p \end{pmatrix} = H_p \begin{pmatrix} x \\ y \\ z \end{pmatrix}$ and the subscript p denotes

the predicted values based on the predicted values for the function H. The Levenberg-Marquardt optimization method provides one of the fastest convergence rates among other techniques [16]. Computational details and stability of different methods [15] to camera calibration is explained in [17].

Interior calibration results of the aforementioned camera set at a focal length of 18 mm are listed in Table (1). Image rectification is the process whereby an image is transformed back into the measurement plane (the plane $z = 0$ of the WCS). Rectified images do not possess any perspective or lens distortions. By placing the calibration object in the measurement
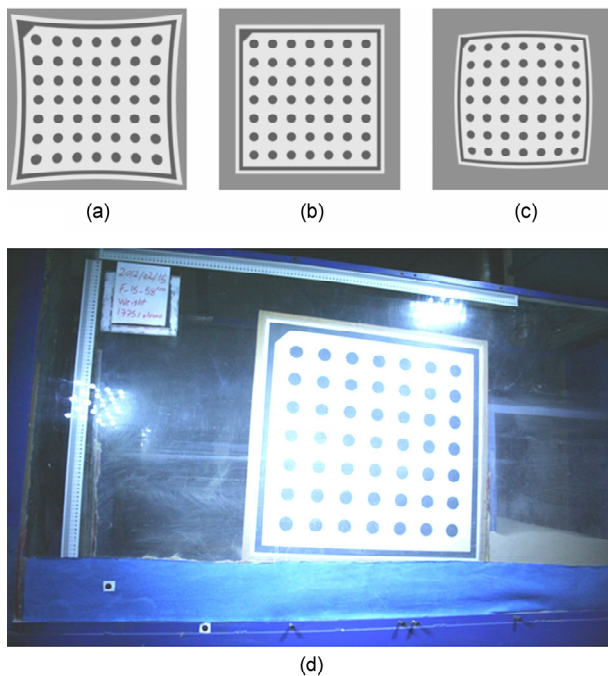

(a)   (b)   (c)

(d)

Figure 5. Effect of distortion modelled with division model with a) $\kappa > 0$ (left), b) $\kappa = 0$ (middle), c) $\kappa < 0$ (right) d) calibration plate using in each test.

Table 1. The interior calibration parameters of the Canon EOS 350D camera.

Parameter	Value
Focus, f	24.907 mm
Kappa, κ	-163.986
S_x	6.428 µm
S_y	6.420 µm
C_x	1689.33 pixel
C_y	980.83 pixel
Image Width	3456 pixel
Image Height	2304 pixel

plane, the resultant rotation and translation matrices correspond to the inverse transformation from CCS to WCS. A sample image along with its corresponding rectified image is shown in the Figure (6). There are two red points above the foundation whose positions are measured in each picture so that the foundation rotation can be calculated accordingly.
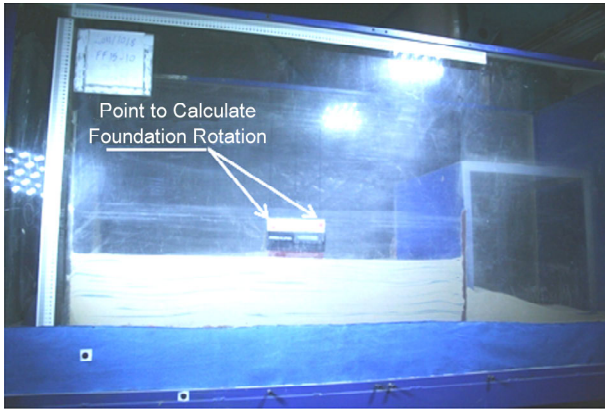
(a)
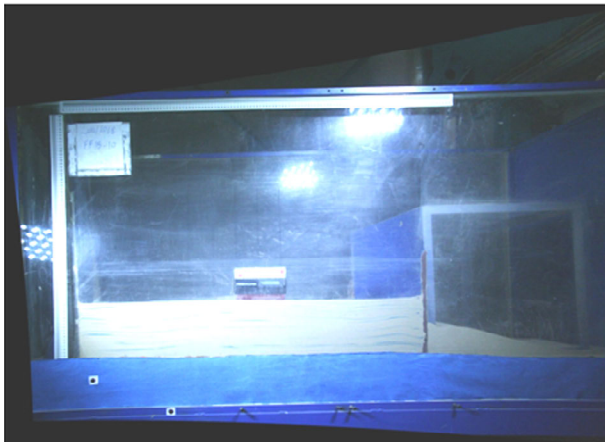
(b)

Figure 6. Comparison between the distorted and rectified image a) Distorted image b) rectified images. Note the perspective change between the two images

3.2. Optical Flow Method

Optical flow is the apparent visual motion of brightness patterns in the image, which can arise from relative motion of objects and/or the viewer itself. Optical flow computations determine motion direction and velocity at possibly all image points. The optical flow represents the image changes due to motion during a time interval *dt*, and the flow field is the velocity field representative of the 3D motion of object points across a 2D image [18] when the viewer is stationary. The computation of optical flow is traditionally based on the hypothesis that intensities of local time-varying image regions are approximately constant under motion for at least a short duration [19]. Mathematically, if $I(x,t)$ is the image intensity function in time and 2D space, then

$$I(x,t) \approx I(x+\delta x, t+\delta t) \qquad (8)$$

where δx is the displacement of the local image region at (x, t) after time. Using a Taylor series expansion of the left hand side of the equation yields:

$$I(x+\delta x, t+\delta t) = I(x,t) + \nabla I \times \delta x + \delta t \times I_t + O^2 \qquad (9)$$

where $\nabla I = (I_x, I_y)$ and I_t are the first-order partial derivatives of $I(x,t)$, and O^2 represents the second and higher order terms of negligible importance. This equation, when trimmed, may be shown as:

$$\nabla I \times \frac{\delta x}{\delta t} + I_t = 0 \quad \text{or} \quad \nabla I \times v + I_t = 0 \qquad (10)$$

where $\nabla I(I_x, I_y)$ is the spatial intensity gradient and $v(u, v)$ is the image flow velocity. It follows from this equation that the intensity change in time, I_t, at the same location of the image is a product of spatial intensity change and flow velocity in this location according to the observer. However, this equation does not completely describe the flow velocity vector and yields only the motion component in the direction of local gradient of the image intensity. This phenomenon is known as the aperture problem and necessitates enforcing other constraints to fully recover the motion.

The computational techniques to optical flow, see Eq. (10), may be generally classified into intensity-based differential methods, frequency-based filtering methods and correlation-based methods [19]. Particle image velocimetry (PIV) is a correlation-based block matching technique used for calculation of deformation patterns and falls into the category of correlation-based optical flow methods. PIV defines image displacement as a shift that obtains the best fit between contiguous time-varying image patches. Matching image patches often requires maximizing a similarity function correlating two corresponding image patches. Typically, a sum of squared differences (SSD) is used as the similarity function. Non-hierarchical PIV algorithms are susceptible to false matches in the presence of large displacements [19].

Beauchemin and Barron [19] work is an informative survey on a wide array of approaches to the computation of optical flow, as well as hypotheses and assumptions they make. Despite their differences, many approaches to optical flow computation consist of three stages of processing [19-20]:

i) Pre-filtering and smoothing with low-pass/band-pass filters to extract signal of interest and to enhance signal to noise ratio,

ii) Extraction of spatiotemporal derivatives (to measure the normal components of velocity) or local correlation surfaces,

iii) The integration of these measurements to produce 2D flow field based on typical assumptions about the underlying flow field smoothness.

In this paper, we have used the recent approach proposed by [21] that combines three assumptions of intensity constancy, gradient constancy and a discontinuity-preserving spatiotemporal smoothness constraint. To allow for large displacements, this approach avoids linearizing the Eq. (6) and uses a variational, multi-scale, coarse-to-fine computational framework. The gradient constancy assumption allows slight changes in brightness to occur and is expressed as:

$$\nabla l(x,t) \approx \nabla l(x, \delta x, y + \delta t) \qquad (11)$$

Again this equation is not linearized. To avoid the aperture problem, the smoothness assumption is introduced into the model. This method is shown to give significantly smaller angular errors than previous methods and is fairly insensitive to parameter variations [21].

Following the computation of optical flow on the series of image taken from the experiment, the relative displacements of soil particles are obtained. By tracking relative displacements with respect to the initial frame, one can compute the absolute particulate displacements. Since the camera is calibrated, all images may be rectified prior to any computation in order to produce displacements in metric unit. The next section shows how these displacements may be used to calculate the strain field across all image points.

3.3. Strain Measurement

Particle displacements measured by optical flow are used to estimate the strain field of the material at hand. Assuming that sand is a continuum, when subject to deformation, its particles move along various paths in space. In our problem, which we work with uniform sand, it is a valid assumption to assuming the sand as a continuum media. It should be mentioned that we don't observe any crack in our experiment. It is an acceptable assumption in nonlinear soil mechanics which can interpret sand behaviour during loading. This motion may be expressed by the following equation:

$$x_i = x_i(X_1, X_2, X_3, t) = x_i(X,t) \quad \text{or} \quad x = (X,t) \qquad (12)$$

This equation shows the current location of x_i of the particle that occupied the point (X_1, X_2, X_3) at time $t = 0$. This description of motion or deformation is the well-known Lagrangian formulation. It can be shown that the second-order Lagrangian (or Green's) finite strain tensor can be expressed by Theory and problems of continuum mechanics [22]:

$$L_{ij} = \frac{1}{2}\left(\frac{\partial x_k}{\partial X_i} \frac{\partial x_k}{\partial X_j} - \delta_{ij} \right) =$$

$$\frac{1}{2}\left(\frac{\partial u_i}{\partial X_j} + \frac{\partial u_j}{\partial X_i} + \frac{\partial u_k}{\partial X_i} \frac{\partial u_k}{\partial X_j} \right) \qquad (13)$$

In small deformation theory of continuum mechanics, the displacement gradients are considered small compared to unity. If these gradients are small, the finite strain tensor reduces to infinitesimal strain tensor:

$$I_{ij} = \frac{1}{2}\left(\frac{\partial u_i}{\partial X_j} + \frac{\partial u_j}{\partial X_i} \right) \qquad (14)$$

Similar to reference [13], constant-strain triangular (CST) elements were used for calculation of displacement and strain fields through the whole medium. Use of these elements avoids the numerical difficulty by evaluating the strain by a grid of three point triangles [13]. The software program is able to compute both types of strains depending on the user's selections.

3.4. Validation

An approximate area of 140 cm in width by 100 cm in height is being imaged in the test procedure. The imaging sensor is capable of showing this physical area in 3456 by 2304 square pixels in each image. Hence, in theory, each pixel in the image

is capturing about 0.4 mm of the physical world. This number may be interpreted as the maximum achievable accuracy of the imaging technique. However, the brightness variation noise induced from imperfect lighting, computational errors due to calibration procedure, hand-induced vibrations when taking images, image processing technique error, and errors from other unknown sources, all contribute to the overall accuracy of the system. To validate the software results, two methods are used: a) Comparison of foundation rotation, measured by the electronic device above the foundation, with that of the image processing technique was satisfactory. Besides, foundation dimensions were compared with their true values from rectified images. b) Synthetic motion sequences were made and the method was tested on them. The optical flow method produced the correct answers that matched that of the synthetic motion. The Figure (7) shows one of the synthetic images similar to the problem at hand.
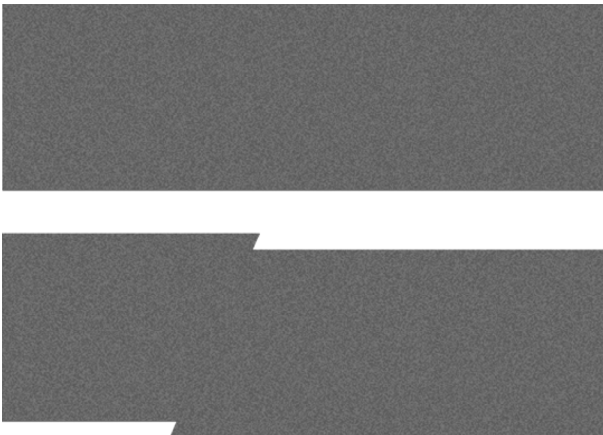

Figure 7. Validation of program results by comparing the results of two moving block.

Experimental measurements showed that the rectified image has an error of 1 mm in the domain of interest, which is very good compared to the theoretical maximum accuracy. The domain of interest represents the central part of the image where the calibration plate is imaged most in the calibration procedure, therefore the numerical solutions to the calibration equations are almost correct in this area and tend to deviate in other farther areas of the image. The rotation of prototype foundation is measured in the rectified image with pixel units rather than metric units and experiments showed an accuracy of 0.1 degrees.

4. Numerical Simulation

The problem was also modelled numerically, employing the validated finite element (FE) method compared with physical modelling. Up to now, numerical model cannot capture all aspects of this problem, but it can be used to reproduce acceptable fault rupture propagation path in the free field [e.g. 23-25] and to capture important aspects of its interaction with shallow and deep foundation.

To have reasonable results, the numerical model should obey some requirements [25]. These requirements include the use of proper constitutive soil model, refined mesh, and special element between soil and foundation.

The problem is modelled with ABAQUS in 2D, assuming plane strain conditions. This program is very powerful in modelling nonlinear behaviour of soil. Additionally, it has special interface element that permits the foundation to slide or detach from the soil during the fault rupture. Following the findings of previous studies [23], an elastoplastic constitutive model with Mohr-Coulomb failure criterion and isotropic strain softening were used. In this model, strain softening is commenced by reducing the mobilized friction angle φ_{mob} and the mobilized dilation angle Ψ_{mob} with the increase of plastic octahedral shear strain, where φ_p and φ_{res} are the peak mobilized friction angle and its residual (or critical state) value, Ψ_p is the peak dilation angle. For further information about this model and its validation, see reference [23]. In real model, we assume that elastic modulus of soil increases with depth. Quadrilateral elements with dimension $d_{FE} = 0.5$ m was used to have reasonable fine mesh.

Linear elastic beam elements are used to model the slab foundation which is positioned on the top of the soil. Foundation is connected to the soil with interface element, which can transmit compression, but it is tensionless and allows the foundation to detach from the soil. The interface between soil and foundation also permits a slippage following Coulomb's friction law. Both detachment and slippage are important phenomena for realistic foundation modelling.

The bottom boundary divides into two parts: one remains stationary representing the footwall, and the other is subjected to the movement of the hanging wall. The large displacement by Lagrangian description was adopted because of the large dislocation imposed.

5. Results

To compare the influence of lightly-loaded and heavy-loaded surface foundation, the results of reduced-scale physical model tests are compared with FE analysis results. This offers combined evidence on the performance of physical modelling, and additional verification of the numerical analysis method employed herein.

5.1. Free-Field Fault Rupture Propagation

At first, results from the free field test are discussed as a reference for the interaction tests. The deformed soil model, see Figure (8a), with superimposed displacement vectors (as computed through image processing) is compared with the *FE* deformed mesh, for bedrock fault offset *h* = 0.6m. Unless otherwise stated, all results are presented in prototype scale. The analysis seems to agree qualitatively with the test, predicting the rupture path and the location of its emergence at the ground surface with acceptable accuracy.

Figure (8b) compares the experimental results with the numerical one in terms of vertical displacement profiles at the ground surface. A reasonable agreement between numerical and experimental

results is observed. The only discrepancy refers to the position and gradient of the surface scarp near the crest of these two models. This discrepancy is attributable to the very low confining pressures in the (1 g) test, the associated increased friction and dilation angle (compared to prototype conditions), and the simplified modelling of post peak soil behaviour.

5.2. Fault Rupture: Soil-Foundation Interaction

To focus on the effect of superstructure weight, we compare the response of the same foundation subjected to surcharge load $q=30$ and $75\,\text{kPa}$ positioned at $s/B=0.3$.

5.2.1. Bearing Pressure of q=30 kPa

Due to the weight of the foundation, the rupture trace is a little shifted to the left edge of the foundation comparing to the free field case. Figure (9) shows digital image captured after a fault movement of 2 m. After the fault movement, shear bands are formed in the sand layer. This shear band began to travel towards the centre of the foundation. In this experiment an area of loss of support (i.e. a gap underneath the foundation) can be clearly observed
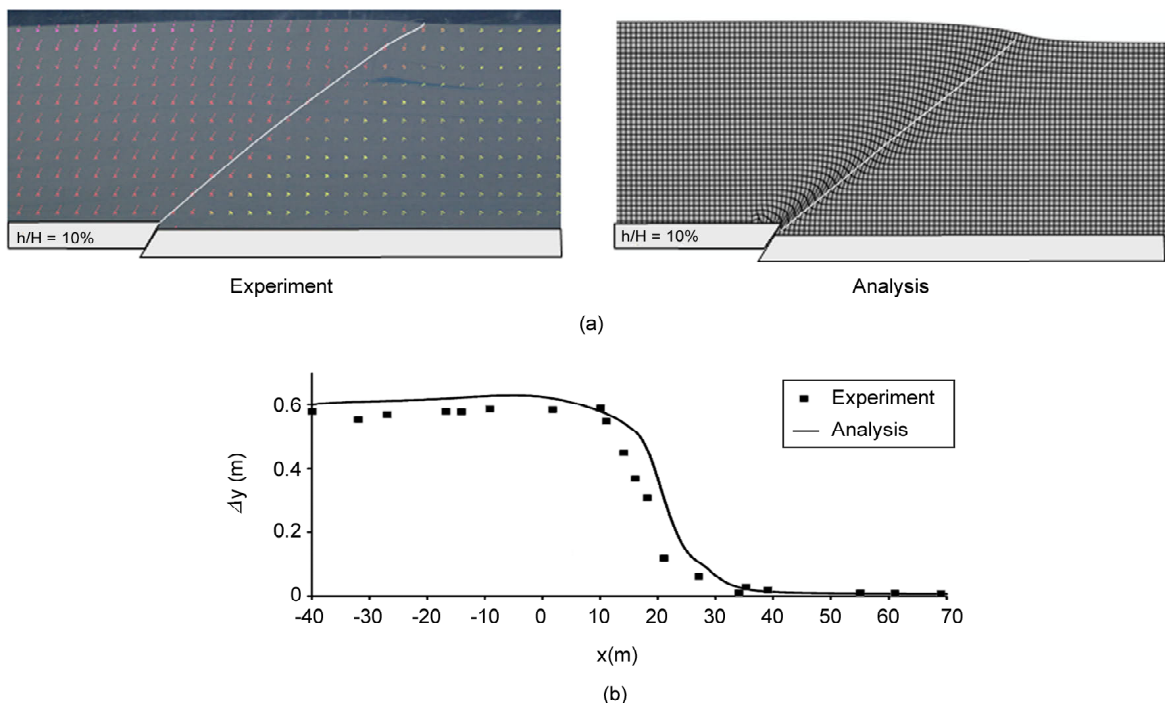

Figure 8. Free-field thrust fault rupture propagation through dense sand. Comparison of experimental with numerical analysis results: (a) photo of the deformed model with superimposed displacement vectors computed through image analysis, compared to FE deformed mesh for bedrock fault offset h = 0.6 m; (b) vertical displacement profiles at the soil surface for fault offset of 0.6m.
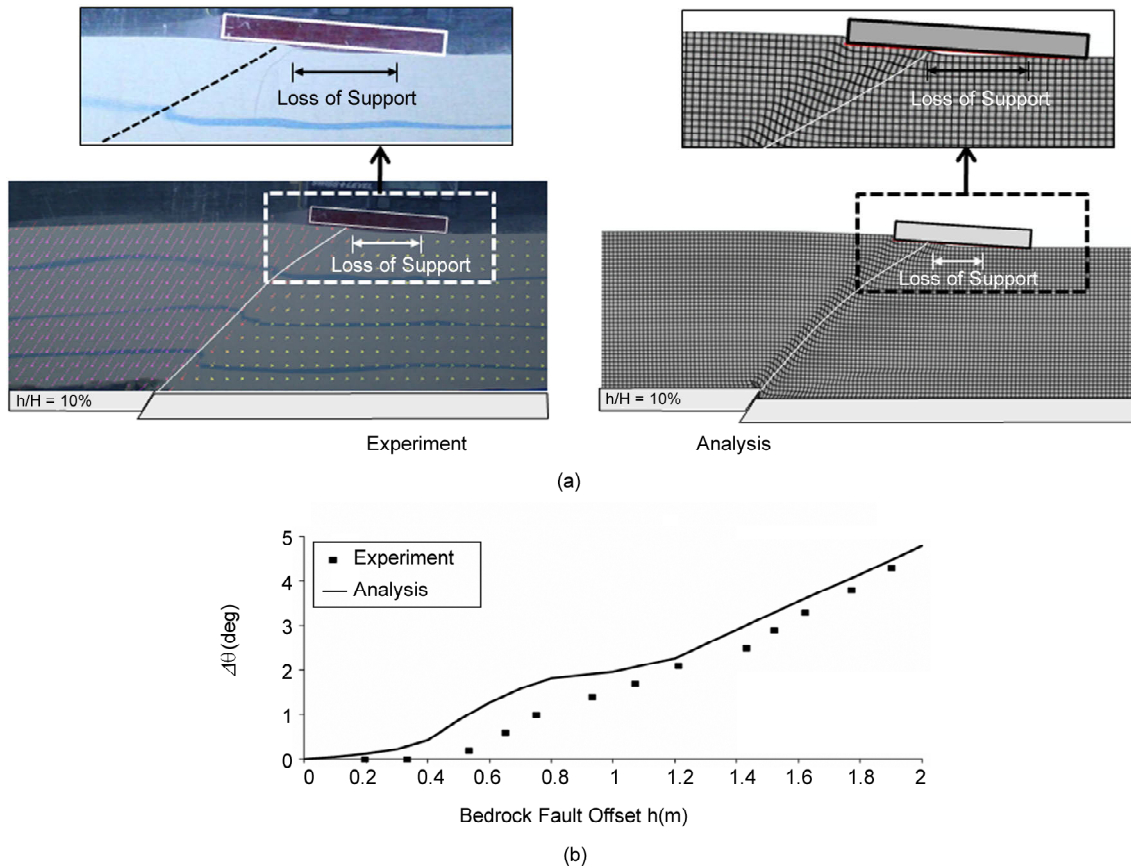
Figure 9. Interaction of a reverse fault rupture propagating through loose sand with a B = 15 m foundation positioned at s/B = 0.3. Comparison of experimental with numerical analysis results: (a) photo of the deformed model with superimposed displacement vectors computed through image analysis, compared to FE deformed mesh for bedrock fault offset h = 2 m; (b) evolution of foundation rotation ϑ with imposed fault offset h.

in Figure (9a). The numerical analysis also seems to predict a foundation detachment. Despite some qualitative difference, the numerical prediction is also in very good agreement with the experiment in terms of foundation rotation, see Figure (9b). The latter reaches almost 5° for bedrock fault offset $h = 2$ m (or $h/H = 10\%$ in dimensionless terms).

5.2.2. Bearing Pressure of q =75 kPa

In the third test presented here, the foundation bearing pressure was increased up to 75 kPa. As shown in Figure (10a), the pressure effectively diverts the fault rupture towards the hanging wall. Almost the same result is obtained through the numerical analysis, which can be seen to agree quite well with the experiment. As a result, the foundation maintains its full contact with the bearing soil (no gapping is observed). Moreover, with the foundation remaining on the footwall, though practically unaffected by the upward displacement of the hanging wall, the resulting foundation rotation ϑ is also

substantially reduced, not exceeding 2° for $h = 2$ m, Figure (10b).

Comparing the results with Figures (9) and (10), it can be concluded that the increase of the surcharge load has a beneficial effect on the diversion of the rupture path. The increase of the surcharge load leads to more intense diversion of the left branch of the fault rupture towards the hanging wall and flattening of the ground deformation underneath the foundation. As a result, the area of loss of support practically vanishes.

6. Summary and Conclusions

In this study, at first, a novel image processing technique was developed for computation of displacements and strain based on theories of optical flow and camera calibration. Vertical and horizontal displacements at different positions within the specimen were computed through image analysis, using custom-developed optical flow software. The latter compares successive digital images to compute the
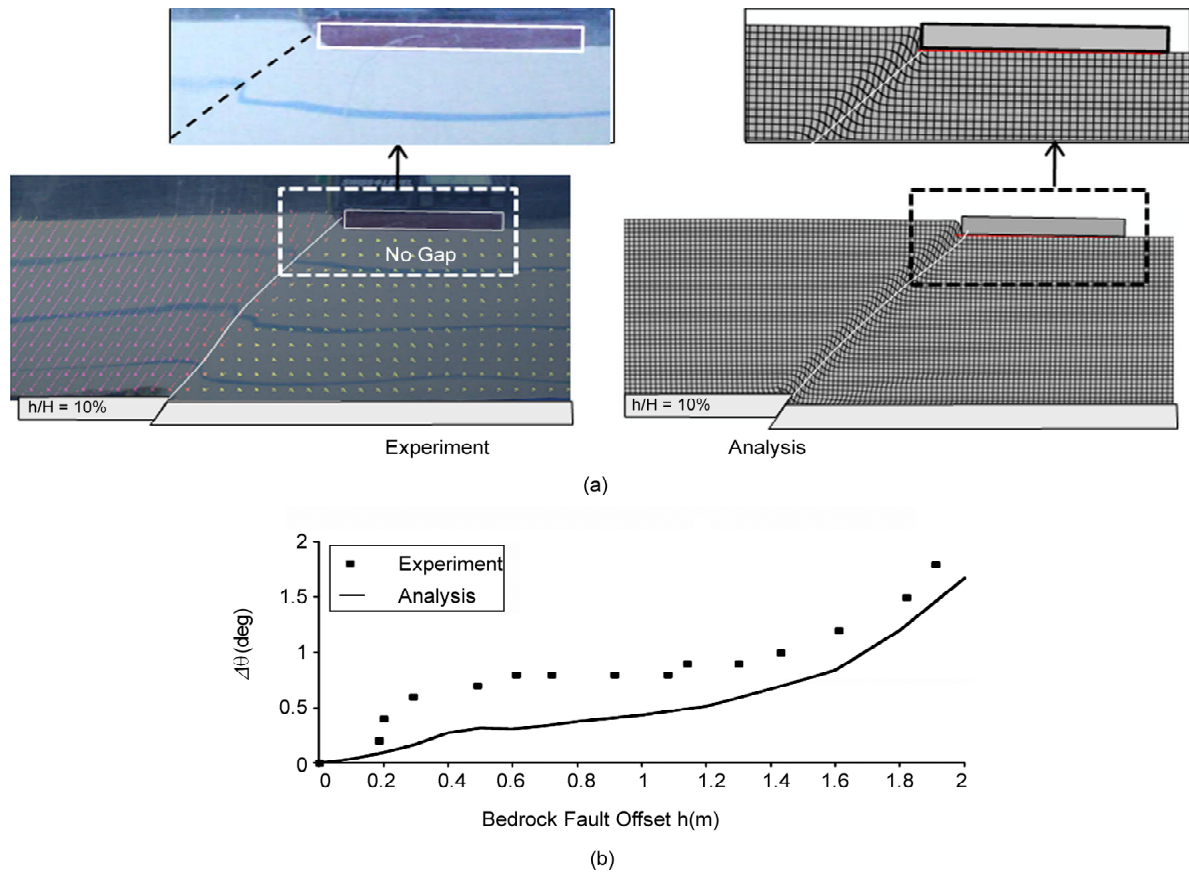
Figure 10. Interaction of a reverse fault rupture propagating through loose sand with a B = 15 m foundation positioned at s/B = 0.3. Comparison of experimental with numerical analysis results: (a) photo of the deformed model with superimposed displacement vectors computed through image analysis, compared to FE deformed mesh for bedrock fault offset h = 2 m; (b) evolution of foundation rotation ϑ with imposed fault offset h.

displacement pattern, in a manner, quite similar to the well-known Geo-PIV software of White et al [15]. Displacement profiles were also computed through additional post-processing. The method is best suited for non-contact full-domain measurements of displacement and strain field in geotechnical settings. Experimental results proved that the methodology is able to robustly determine the fault rupture zone in sand box tests. By using this powerful means, the influence of increasing the weight of the superstructure, expressed here in a simplified way with the surcharge load q, was investigated. The increase of surcharge load has several advantages: (a) it changes the stress field underneath the foundation, causing the diversion of the fault rupture. It should be mentioned that beneficial effect of increasing surcharge weight to divert the rupture path is investigated in homogeneous soil; and (b) heavy bearing pressure foundation by compressing the soil, tends to smooth the faulting-induced scarps or anomalies of the ground surface as a kinematic constrain. Hence, the foundation separation dimin-

ishes rapidly by increasing surcharge load. The present paper deals with the quasi-static offset due to fault offset, and the related seismic motion is not considered. Such combined stressing has not been addressed in the present work, and further research is desirable.

References

1. Faccioli, E., Anastasopoulos, I., Callerio, A., and Gazetas, G. (2008). Case Histories of Fault-Foundation Interaction, Bulletin of Earthquake Engineering, **6**(4), 557-583.

2. Anastasopoulos, I. and Gazetas, G. (2007a). Foundation-Structure Systems Over a Rupturing

Normal Fault: Part I. Observations after the Kocaeli 1999 Earthquake, Bulletin of Earthquake Engineering, **5**(3), 253-275.

3. Lin, A., Ren, Z., Jia, D., and Wu, X. (2009). Co-Seismic Thrusting Rupture and Slip Distribution Produced by the 2008 Mw 7.9 Wenchuan Earthquake, China, *Tectonophysics*, **471**, 203-215.

4. Xu, X., Yu, G.Y., Klinger, G., Chen, G., Feng, X., Li, C., Zhu, A.,Yuan, R., Guo, T., Sun, X., Tan, X., and An, Y. (2010). Fault-Scarp Features and Cascading-Rupture Model for the Mw 7.9 Wenchuan Earthquake, Eastern Tibetan Plateau, China, Bulletin of the Seismological Society of America, **100**(5B), 2590-2614.

5. Anastasopoulos, I. and Gazetas, G. (2007b). Behavior of Structure-Foundation Systems Over a Rupturing Normal Fault: Part II, Analysis of the Kocaeli case histories, Bulletin of Earthquake Engineering, 5(3), 277-301.

6. Moosavi, S.M., Jafari, M.K., Kamalian M., and Shafiee, A. (2010). Experimental Investigation of Reverse Faul Rupture-Rigid Shallow Foundation Interaction, *International Journal of Civil Engineering*, **8**(2), 85-98.

7. Lee, J.W. and Masanori, H. (2005). An Experimental Study on Earthquake Fault Rupture Propagation through a Sandy Soil Deposit, *Structural Engineering/Earthquake Engineering*, 22(1), 1s-13s.

8. Bransby, M.F., Davies, M.C.R., El Nahas, A., and Nagaoka S. (2008). Centrifuge Modeling of Reverse Fault-Foundation Interaction, Bulletin of Earthquake Engineering, **6**(4), 607-628.

9. Bransby, M.F., Davies, M.C.R., and El Nahas, A. (2008). Centrifuge Modeling of Normal Fault-Foundation Interaction, Bulletin of Earthquake Engineering, 6(4), 585-605.

10. Anastasopoulos, I., Antonakos, G., and Gazetas, G. (2010). Slab Foundations Subjected to Thrust Faulting: Parametric Analysis and Simplified Design Method, *Soil Dynamics & Earthquake Engineering*, **30**(10), 912-924.

11. Paolucci, R. and Yilmaz, M.T. (2008). Simplified theoretical Approaches to Earthquake Fault Rupture-Shallow Foundation Interaction, Bulletin of Earthquake Engineering, **6**(4), 629-644.

12. Yilmaz, M.T. and Paolucci R. (2007). Earthquake Fault Rupture-Shallow Foundation Interaction in Undrained Soils: A Simplified Analytical Approach, *Earthquake Engineering and Structural Dynamics*, **36**(1), 101-118.

13. White, D.J. (2002). An Investigation into the Behavior of Pressed-in Piles, Ph.D. Thesis, Churchill College, University of Cambridge.

14. Anastasopoulos, I., Georgarakos, T., Georgiannou, V., Drosos, V., and Kourkoulis, R. (2010) Seismic Performance of Bar-Mat Reinforced-Soil Retaining Wall: Shaking Table Testing Versus Numerical Analysis with Modified Kinematic Hardening Constitutive Model, *Soil Dynamics and Earthquake Engineering*, **30**(10), 1089-1105.

15. Horn, B.K.P. (2000). Tsai's Camera Calibration Method Revisited, Massachusetts Institute of Technology.

16. Heikkila, J. and Silven, O. (2002). Calibration Procedure for Short Focal Length Off-the-Shelf CCD Cameras, *Proc. of the 13th International Conference on Pattern Recognition*.

17. Gonzalez, I., Gamez, J.C., Artal, C.G., and Cabrera, A.M.N. (2005). Stability Study of Camera Calibration Methods, CI Workshop en Agentes Fisicos, Spain.

18. Sonka, M., Hlavac, V., and Boyle, R. (2008). Image Processing, Analysis and Machine Vision, 3rd Ed., Thompson Learning.

19. Beauchemin, S.S. and Barron, J.L. (1995). The Computation of Optical Flow, *ACM Computing Surveys*, **27**(3), 433-467.

20. Barron, J.L., Fleet, D.J., and Beauchemin, S.S. (1994). Performance of Optical Flow Techniques, International Journal of Computer Vision.

21. Brox, T., Bruhn, A., and Wickert J. (2004). High Accuracy Optical Flow Estimation Based on a Theory for Warping, *Proc. 8th European Conf. on Computer Vision*.

22. Chen, W.F. and Mizuno, E. (1990). Nonlinear Analysis in Soil Mechanics, Elsevier Science Publishers.

23. Anastasopoulos, I., Gazetas, G., Bransby, F., Davies, M.C.R., and El Nahas, A. (2007). Fault Rupture Propagation through Sand: Finite Element Analysis and Validation through Centrifuge Experiments, *Journal of Geotechnical and Geo Environmental Engineering, ASCE*, **133**(8), 943-958.

24. Loukidis, D. and Bouckovalas, G. (2001). Numerical Simulation of Active Fault Rupture Propagation through Dry Soil, *Proc. 4th International Conference on Recent Advances in Geotechnical Earthquake Engineering and Soil Dynamics and Symposium in Honor of Professor W.D. Liam Finn*, San Diego, CA, 26-31.

25. Bray, J.D. (1990). The Effects of Tectonic Movements on Stresses and Deformations in Earth Embankments, PhD Dissertation, University of California, Berkeley.